Dynamical control for capturing vortices near bluff bodies

Áron Péntek* and James B. Kadtke
Institute for Pure and Applied Physical Sciences, University of California, San Diego, 9500 Gilman Drive, La Jolla, California 92093-0360

Gianni Pedrizzetti
Dipartimento di Ingegneria Civile, Università di Firenze, via Santa Marta 3, 50139 Florence, Italy
(Received 20 January 1998)

We investigate the vortex dynamics near a translating and rotating circular cylinder in a two-dimensional uniform viscous flow. In analogy with the point-vortex and Eulerian dynamics, there is an interesting scattering effect of vortices approaching the cylinder from far upstream. The vortex–boundary-layer interaction plays an important role in the scattering processes. We implement a modified Ott, Grebogi, and Yorke chaos control scheme, based on a low-dimensional Hamiltonian model of the flow, to capture and stabilize a concentrated vortex around the cylinder. This point-vortex-based control model can successfully be applied in a viscous flow when control is actuated by uniformly rotating the cylinder and actively changing the background flow velocity far from the body. We demonstrate that such a control mechanism can simultaneously control the vortex dynamics, and also suppress the vortex shedding. An analysis of the vortex–boundary-layer interaction is presented to explain the absence of vortex shedding during control simulations. [S1063-651X(98)10508-1]

PACS number(s): 47.32.Cc, 05.45.+b, 47.52.+j, 83.50.Ws

I. INTRODUCTION

The interaction of fluid flows and vortical structures with embedded bodies is an important research area in fluid mechanics, with widespread applications in hydrodynamics and aerodynamics, and structural engineering problems. In recent years, considerable effort has been made to control such fluid flows in order to improve the flow characteristics. The possible applications include wake stabilization, lift enhancement, drag and noise reduction, and mixing enhancement, and are attracting increasing interest [1–5].

The complexity of such control problems leads to the study of reduced low-dimensional flow models, which in certain limits capture most of the qualitative features of vortex-body interaction [6–11]. These models provide a framework where an active control algorithm can be easily developed and understood, before it is applied in a realistic fluid system [i.e., full Navier-Stokes (NS) equations]. More importantly, recent advances in control theory of dynamical systems can naturally be applied in these reduced low-dimensional fluid systems. In particular, the method developed by Ott, Grebogi, and Yorke (OGY) [12] has already proven to be successful in several applications, such as controlling a magnetoelastic ribbon [13], a thermal convection loop [14], chemical reactions [15], solid state devices [16], and chaotic lasers [17].

One of the simplest models for the interaction of a bluff body with concentrated fluid vorticity is that of a single Hamiltonian point vortex interacting with a two-dimensional (2D) cylinder. This system has been extensively studied [18], and it is known to exhibit several remarkable features including a chaotic capturing phenomenon. It has been shown previously [8] that by a proper control algorithm such a vortex can be stably captured near the cylinder. A more interesting result is that the controlled capture can successfully be implemented even for a distribution of vorticity, at corresponding parameter regimes [8]. In this work a continuous vorticity distribution was evolved according to the NS equations, coupled with inviscid ''free-slip'' boundary conditions on the cylinder surface. This approach, which essentially simulates an inviscid evolution and avoids some numerical difficulties, was aimed to study the qualitative correspondence of Hamiltonian dynamics for continuous fields.

Our aim in this paper is to similarly analyze the dynamics of coherent vortical structures approaching a rotating cylinder in a viscous fluid at Reynolds number around $\mathrm{Re}=1000$, and to develop a possible control mechanism to stably capture a vortex around the cylinder. First, we show that there is an interesting vortex scattering effect, and even a vortex capturing phenomenon, in the case of a rotating cylinder. These phenomena have been previously pointed out in the Hamiltonian vortex dynamics and in the inviscid flow. In the viscous case, however, they have a completely different physical origin: the vortex–boundary-layer interaction, which plays an important role in the vortex dynamics.

Secondly, we demonstrate that by proper perturbations to the flow it is possible to control a vortex passing by a cylinder. The basic requirement we impose for such a control algorithm is that it be implemented only through physically motivated boundary conditions. This leads essentially to two mechanisms in the framework of our model system: one can either rotate the cylinder and/or change the uniform background flow velocity far from the body (i.e., the translational velocity of the cylinder). The other parameters of the problem, such as the circulation around the body or the vortex strength, are not experimentally accessible parameters in a realistic viscous flow, and thus they cannot be used for control. Other forms of control, such as blowing and suction on the cylinder surface, are not studied in this paper. They are,

*Also at Department of Physics, University of California, San Diego, La Jolla, CA 92093-0319.

however, likely candidates for alternative control actuators, as they have been used with success in other flow control problems [7]. In this paper we use small changes in the uniform background flow velocity far from the body as control actuator. We show that these perturbations combined with a uniform rotation of the cylinder can successfully control the vortex and simultaneously stabilize the boundary-layer dynamics.

In our analysis we first review the Hamiltonian vortex dynamics, and implement the control algorithm for the point-vortex system by using perturbations of the background flow velocity far from the body. In order to clearly understand what the particular effects of the finite-size vortex patch, of the diffusion of vorticity, and of the vortex–boundary-layer interaction on the vortex dynamics and control in a viscous flow are, we review in some detail the free-slip vortex dynamics. The free-slip numerical simulations are designed to understand the vortex dynamics and control for a vortex patch in the presence of viscosity but without a boundary layer on the cylinder surface. Next, we analyze the vortex dynamics in a viscous flow around a rotating cylinder, and show the influence of the boundary layer on the vortex dynamics. Finally, these results are used to develop the control procedure for the vortex dynamics.

This paper is organized as follows. In the next section the vortex dynamics and control problem is formulated for Hamiltonian point-vortex dynamics. Section III is devoted to the numerical procedure for solving the Navier-Stokes equations for free-slip and no-slip dynamics. In Sec. IV an analysis of the free-slip vortex scattering and control is presented. Section V is devoted to the vortex scattering dynamics in a viscous flow. The control algorithm for the viscous case is described in Sec. VI. A detailed analysis of the vortex boundary-layer interaction and the stability of the boundary layer during control is presented in Sec. VII. Section VIII contains our concluding remarks.

II. THE HAMILTONIAN MODEL

The Hamiltonian model consists of a circular boundary centered at the origin of the coordinate system, embedded in a uniform background flow of velocity u_0 parallel to the x axis and pointing in the negative x direction (Fig. 1). We also assume a possible varying perturbation δu_0 to the uniform background flow velocity. A point vortex of circulation κ is advected past the cylinder by the background flow, starting upstream of the cylinder. In nondimensional polar coordinates (r,θ), scaled by the cylinder radius R_0 and the background flow u_0, the Hamiltonian for the vortex dynamics is given by [18]

$$H=-(1+\varepsilon)r\left(1-\frac{1}{r^2}\right)\sin\theta+\frac{\sigma}{2}\ln(r^2-1), \qquad (1)$$

where the first term is due to the background flow, and the second term to the flow induced by an image vortex. Here $\sigma=\kappa/2\pi R_0 u_0$ is the nondimensional vortex strength. The parameter $\varepsilon=\delta u_0/u_0$ represents the rescaled perturbation of the background flow. Note that the possible rotation of the cylinder is not included in Eq. (1). This could be modeled by including a uniform circulation around the cylinder. Since,

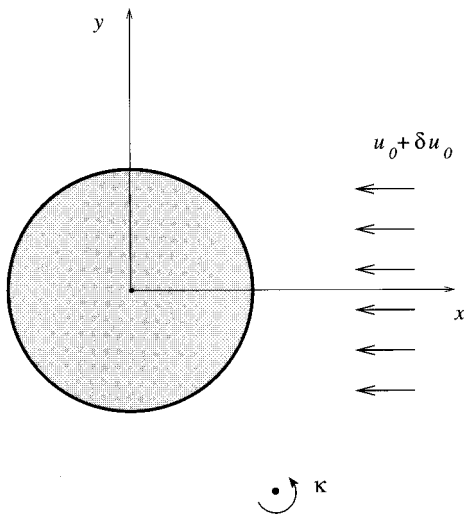

FIG. 1. Schematic diagram of the idealized flow.

however, in the viscous flow we are interested in simulations on time scales much shorter than the typical spin-up time of the fluid around a rotating cylinder, as a first approximation the effect of the cylinder rotation can be neglected if the vortex does not come very close to the cylinder surface.

The equations of motion for the vortex dynamics are of the Hamiltonian form:

$$\dot{r}=\frac{1}{r}\frac{\partial H}{\partial\theta}, \quad \text{and} \quad \dot{\theta}=-\frac{1}{r}\frac{\partial H}{\partial r}. \qquad (2)$$

Equation (2) corresponds to a one degree of freedom autonomous Hamiltonian system that is always integrable. With small, time-dependent perturbations introduced into the background flow, however, Eq. (2) has the same structure as that of a driven one degree of freedom Hamiltonian system that is known to generically exhibit chaos. Thus the vortex approaching the cylinder can be captured and exhibit complicated, chaotic motion around the cylinder for a *finite* time before it is transported away downstream [18,19]. This behavior is a hydrodynamic manifestation of chaotic scattering [20], or more generally, of transient chaos [21].

A detailed analysis of the phase space of the above system reveals a simple flow topology [18]. To illustrate our control strategy, we choose a simple autonomous system with fixed $\sigma=-2.962\,96$, and $\varepsilon=0$ that produces a single saddle point at $(0,-3)$ in Euclidean coordinates [Fig. 3(a)]. The control technique presented in this paper is independent of the specific choice of the parameter σ. The technique relies on the existence of at least one saddle point which can be found at any parameter regime. The solid lines in Fig. 3(a) are the constant energy lines of the Hamiltonian (1). Since the energy is conserved during the motion, they also correspond to the vortex trajectories. We emphasize that these lines are not the stream lines of the flow. The stream-line pattern depends on the actual vortex position, and is changing in time as the vortex is advected past the cylinder.

Our aim here is to capture and stabilize the passing vortex at this fixed point by utilizing the OGY method of chaos control. Briefly, the OGY method stabilizes one of the many unstable periodic orbits or fixed points which are inherently present in the dynamics of the system. For unstable fixed

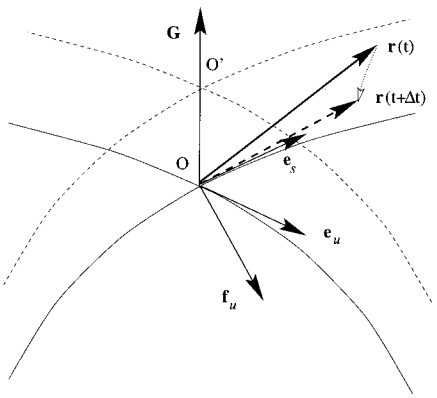

FIG. 2. Schematic diagram of the saddle point O and its stable and unstable manifolds (solid lines) in the phase space. Under small perturbations the fixed point moves along $\mathbf{G}$ to O'. The control algorithm requires a perturbation that brings the original point $\mathbf{r}(t)$ close to the stable manifold. The perturbed system is shown by dashed line. Due to the applied control the trajectory approaches the stable manifold of the unperturbed system along the dotted line.

points of hyperbolic character (also called saddle points) there exists a curve along which the fixed point can be exactly reached, named the stable manifold [12]. The control consists of small perturbations applied in such a way as to drive the actual trajectory close to the stable manifold of the desired orbit (cf. Fig. 2). In this way, we take advantage of the naturally attractive dynamics around the stable manifold to reach the unstable fixed point. Since the stable manifold is typically a set of measure zero, and it cannot be reached exactly, control is repeated at discrete time steps Δt to apply corrections. Here we will restrict ourselves to controlling a single fixed point, and not the full transient chaotic dynamics. The method is nevertheless the same, and can be directly applied for the chaotic case as well.

The control procedure described above is capable of controlling the vortex dynamics if the vortex initially starts in the vicinity of the fixed point, where a linear approximation of the dynamics is valid [12]. In open flows, however, the probability that the vortex will pass by a close neighborhood of the fixed point is typically very small. Only a small fraction of initial conditions lying around the stable manifold satisfy this condition. To demonstrate this one could start with a large number of initial conditions and wait until one of them falls in the preselected neighborhood of the desired orbit, as transient chaos has been first controlled [22]. Alternatively one can implement a targeting algorithm [23] that drives the vortex to the fixed point, not necessarily with small perturbations.

Such a targeting algorithm has been proposed in Ref. [8]. It takes advantage of the robustness of the flow topology to large perturbations that is observed in our model system, i.e., the saddle-point-like structure is preserved even for large perturbations. If $\dot{\mathbf{r}}=\mathbf{A}(\mathbf{r},\varepsilon)$ represents the dynamical system of Eq. (2), the dynamics in the vicinity of the fixed point can be approximated by the linearized equation

$$\dot{\delta}\mathbf{r}=\mathbf{J}\delta\mathbf{r}+\mathbf{G}\varepsilon, \tag{3}$$

where the actual vortex position relative to the fixed point is $\delta\mathbf{r}$, and

$$\mathbf{J}=\left.\frac{\partial\mathbf{A}}{\partial\mathbf{r}}\right|_{\delta\mathbf{r}=0,\varepsilon=0} \tag{4}$$

is the Jacobian matrix evaluated at the saddle point. The vector

$$\mathbf{G}=\left.\frac{\partial\mathbf{A}}{\partial\varepsilon}\right|_{\delta\mathbf{r}=0,\varepsilon=0} \tag{5}$$

gives the effect of small perturbations on the dynamical system. After a short evolution time Δt, the new vortex position becomes

$$\delta\mathbf{r}(t+\Delta t)\approx[\mathbf{1}+\mathbf{J}\Delta t]\,\delta\mathbf{r}(t)+\mathbf{G}\Delta t\varepsilon(t). \tag{6}$$

To achieve control, the vortex dynamics is perturbed in such a way that the vortex starting upstream of the cylinder is driven along the stable eigendirection in the vicinity of the fixed point. Let $\mathbf{e}_s$ and $\mathbf{e}_u$ denote the stable and unstable eigenvectors of the Jacobian $\mathbf{J}$, respectively. We define the covariant unstable eigenvector $\mathbf{f}_u$ by the relations

$$\mathbf{f}_u\cdot\mathbf{e}_u=1 \quad \text{and} \quad \mathbf{f}_u\cdot\mathbf{e}_s=0.$$

The size of the perturbation is evaluated from the condition that the projection of $\delta\mathbf{r}$ on the covariant unstable eigenvector $\mathbf{f}_u$ of matrix $\mathbf{J}$ should decrease each time control is applied [Fig. 1(b)], i.e.,

$$\mathbf{f}_u\cdot\delta\mathbf{r}(t+\Delta t)=(1-\beta)\mathbf{f}_u\cdot\delta\mathbf{r}(t). \tag{7}$$

The parameter β is smaller than one, and is chosen to be a function of the distance $|\delta\mathbf{r}|$ in order to control the magnitude of the perturbation during the targeting procedure. The required perturbations ε can then be expressed as a function of the position $\delta\mathbf{r}$ relative to the fixed point in the following way [8]:

$$\varepsilon(t)=-\left(\lambda_u+\frac{\beta}{\Delta t}\right)\frac{\mathbf{f}_u\cdot\delta\mathbf{r}(t)}{\mathbf{f}_u\cdot\mathbf{G}}, \tag{8}$$

where λ_u is the unstable eigenvalue of $\mathbf{J}$. In the present paper an exponential dependence $\beta=\exp(-\gamma|\delta\mathbf{r}|)$ has been used, although the qualitative results are not apparently dependent on the particular functional form.

Figure 3(a) shows the dynamics of a point vortex under the perturbations (8). The parameters $\mathbf{f}_u$, $\mathbf{G}$, and λ_u have been determined analytically from Eqs. (1) and (2). The time evolution of perturbations to the uniform background flow are shown in Fig. 3(b). One can clearly observe that the control algorithm drives the vortex along the stable direction to the saddle point. Except for the initial perturbations during the targeting procedure, only extremely small perturbations are needed to keep the vortex at the saddle point. In the example shown in Fig. 3(b) the maximum value of the perturbation is quite large during the targeting procedure ($\varepsilon_{\max}\approx 1.6$). This is due to the fact that if the dynamics is not chaotic, it is typically not possible to drive the vortex trajectory to the stable manifold by small perturbations only. One can, however, optimize this targeting procedure by properly choosing the $\beta(|\delta\mathbf{r}|)$ function. Depending on the particular objective, one can attempt to either minimize the largest per-

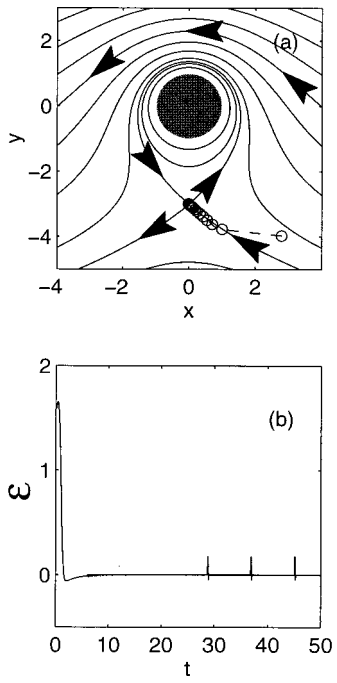

FIG. 3. (a) Typical flow topology: vortex flow lines with arrows indicate direction of the vortex motion. Small circles indicate time evolution of a point vortex under the dynamics of the control and targeting scheme. Initial vortex position is (3.0, −4.0), and $\sigma = -2.962\,96$. The control time interval is $\Delta t = 0.1$ and the targeting parameter $\gamma = 1$. (b) The perturbation to the background flow velocity during control.

turbations or to achieve a smallest cost solution, e.g., by minimizing $\int \varepsilon(t)dt$. Alternatively, in a real fluid system one can also impose restriction on the maximum allowed acceleration of the cylinder, i.e., one can limit $\Delta\varepsilon/\Delta t$ to reflect limitations due to the inertia of the cylinder.

During the control part, the size and frequency of the maximum perturbations [the three spikes in Fig. 3(b)] depend on the precision of measurement of $\delta\mathbf{r}$. Higher precision in $\delta\mathbf{r}$ results in more frequent and smaller magnitude perturbations. If the absolute precision is ζ, the maximum perturbation scales as $\varepsilon_{\max} \sim \zeta(\lambda_u + 1/\Delta t)$, and the time interval between spikes as $\Delta t_{\text{spikes}} \sim (\ln \zeta)/\lambda_u$.

Our aim in this paper is to analyze the corresponding vortex dynamics and control as above in a viscous flow. Due to the complexity of the problem, we first analyze the vortex dynamics with inviscid free-slip boundary conditions, and in a second step we concentrate on the viscous case. The next section details the numerical procedure for both the free-slip and no-slip simulations.

III. NUMERICAL SOLUTION OF NAVIER-STOKES EQUATIONS

In our numerical analysis we use a pseudospectral evolution scheme discussed previously in Ref. [24]. The NS equation is solved using a vorticity-stream function representation (ω, ψ) of the flow implemented on a polar grid centered on the body. The scheme uses a finite-difference approximation in the radial direction and spectral decomposition in the angular direction. The velocity field in polar coordinates (ρ, ϕ) is given by

$$v_\rho = \frac{1}{\rho}\frac{\partial \psi}{\partial \phi} \quad \text{and} \quad v_\phi = -\frac{\partial \psi}{\partial \rho} \tag{9}$$

for the radial and tangential velocities, respectively. The NS equations rendered in dimensionless form are

$$\frac{\partial \omega}{\partial t} = \frac{1}{\rho}\left(\frac{\partial \psi}{\partial \rho}\frac{\partial \omega}{\partial \phi} - \frac{\partial \psi}{\partial \phi}\frac{\partial \omega}{\partial \rho}\right) + \frac{1}{\mathrm{Re}}\nabla^2\omega, \tag{10}$$

$$\omega = -\nabla^2 \psi, \tag{11}$$

where the Reynolds number $\mathrm{Re} = u_0 R_0/\nu$ and ν is the kinematic viscosity.

To ensure high grid density in the physically interesting region (close to the body) a radially stretched grid is introduced. Such a grid maintains high resolution close to the cylinder yet can still extend to large distances, to simulate a real open flow. In particular, we use $\eta = \ln[(r-1+a)/a]$ as the new radial coordinate with a being a stretching parameter.

The main component of the flow field is due to the background flow, and can be derived from the inviscid stream function:

$$\psi_0(\rho, \phi) = -(1+\varepsilon)\rho\left(1 - \frac{1}{\rho^2}\right)\sin\phi. \tag{12}$$

To simplify numerical calculations we rewrite the NS equations to evolve only the corrections to this flow. The resulting equations are somewhat lengthy and are omitted here for brevity. They are, however, identical to those in Ref. [24] and the reader is referred there. The time evolution is computed using a third-order Runge-Kutta scheme with fixed step size [24].

On the outer boundary of the computational domain the boundary conditions are set to match the inviscid solution far from the body, i.e.,

$$\psi(\rho_{\max}, \phi) = \psi_0(\rho_{\max}, \phi). \tag{13}$$

Details of how these boundary conditions are numerically implemented can also be found in Ref. [24].

A. Details of the free-slip simulation

The physical boundary conditions on the cylinder surface are, in the free-slip case,

$$\left.\frac{\partial \psi}{\partial \phi}\right|_{\rho=1} = 0. \tag{14}$$

Numerically this is implemented as $\psi(\rho = 1, \phi) = 0$. Additionally, as suggested in Ref. [25], the numerical boundary condition $\partial\omega/\partial\rho = 0$ is imposed on the cylinder boundary, which correctly reproduces an inviscid dynamics.

As the initial vorticity field for the control simulations, we used a localized Gaussian distribution of vorticity $\sim \exp[(\mathbf{r}-\mathbf{r}_0)^2/2\delta^2]$ centered on a point $\mathbf{r}_0$ far from the cylinder, of typical transversal size δ. The initial position of the Gaussian vortex was in the vicinity of the stable manifold of the fixed point of the background point-vortex model, to avoid artificially large initial perturbation during the target-

ing procedure. The extension δ of the distribution ranges from 0.2 to 0.6, so the size of the vortex is comparable with that of the cylinder.

The position $\mathbf{r}_0(t)$ of this extended vortex, required for the input to the control algorithm, is computed as the center of vorticity in a domain $\mathcal{D}(t)$ around the vortex:

$$\mathbf{r}_0(t+\Delta T)=\frac{\int_{\mathcal{D}(t)}\mathbf{r}'\,\omega(\mathbf{r}')\,\theta(-\omega(\mathbf{r}'))d^2\mathbf{r}'}{\int_{\mathcal{D}(t)}\omega(\mathbf{r}')\,\theta(-\omega(\mathbf{r}'))d^2\mathbf{r}'}, \tag{15}$$

where ΔT is the time step for numerical integration and $\mathcal{D}(t)$ is a disk of radius 2δ centered on the vortex position at time t, i.e., $\mathbf{r}_0(t)$. The function $\theta(\omega)=1$ for $\omega>0$ and $\theta(\omega)=0$ for $\omega<0$, is used to weight the positive vorticity only, avoiding confusion with the opposite-signed shed vorticity (which appears only in the no-slip simulations). In a realistic controller such an input should come from instantaneous physical measurements, such as multiple pressure observations and/or velocity monitoring. It has been shown previously that the vortex dynamics can be entirely reformulated in a pressure-measurement space, by recording two or three point pressures on the cylinder surface [26]. Then a control algorithm analogous to the one described here can be applied in the pressure space without relying on actual vortex position [27].

B. Details of the no-slip simulation

The physical boundary conditions on the cylinder surface are typical no-slip conditions, i.e.,

$$\left.\frac{\partial\psi}{\partial\phi}\right|_{\rho=1}=0 \quad \text{and} \quad \left.\frac{\partial\psi}{\partial\rho}\right|_{\rho=1}=\Omega, \tag{16}$$

where Ω is the angular velocity of the cylinder, measured in the counterclockwise direction. These boundary conditions can be used to specify the stream function and the vorticity at the boundary. As numerical boundary condition for the stream function, $\psi=0$ is used. The value of the wall vorticity is obtained by inserting conditions (16) in Eq. (11), specified at the wall and using a standard second-order estimate [25].

To ensure physically self-consistent initial conditions for the vortex dynamics, and to avoid the transient effects of wake generation during the control process, we first compute the solution for a fully developed wake with no controlled vortex present. To break the initial symmetry of the wake (which is unavoidable for symmetric initial conditions) the cylinder was impulsively rotated back and forth during the first few time units and stopped afterwards. The relaxation toward a periodic solution is checked by monitoring the evolution of forces on the cylinder [cf. Fig. 15(a)].

After this, a Gaussian distribution of vorticity is superimposed on the vortex street solution centered at a point $\mathbf{r}_0$ far upstream of the cylinder. In the numerical scheme this corresponds to a vortex that suddenly enters the finite computational domain. In response to this event the total circulation contained in the domain grows by a quantity equal to the vortex circulation.

This fact cannot be accounted for by the boundary condition (13) which imposes the irrotational field, with zero circulation, on the outer edge of the domain. The artificial constraint of condition (13) would require creation of additional circulation. The only mechanism by which additional circulation can be created is by vortex shedding from the cylinder surface. Thus the placement of the vortex in the computational domain would result in an impulsive vorticity generation and consequent impulsive shedding even if the vortex is placed far from the cylinder. To maintain the circulation balance, condition (13) should be replaced by a condition where the actual value of circulation around the domain is imposed explicitly. Instead, for numerical convenience, this is done by introducing a second vortex of equal strength and opposite sign far downstream which maintains the vorticity balance in the computational domain. This additional vortex does not influence directly the vortex dynamics (it is far from the upstream vortex), but successfully balances the circulation in the computational domain. The position of the vortex placed upstream is monitored in analogy with the free-slip case using Eq. (15).

The drag and lift coefficients C_D and C_L are computed as [28]

$$\begin{aligned} C_D&=\int_0^{2\pi}d\phi(-\tilde{p}\cos\phi-\tilde{\sigma}_{\rho\phi}\sin\phi),\\ C_L&=\int_0^{2\pi}d\phi(-\tilde{p}\sin\phi+\tilde{\sigma}_{\rho\phi}\cos\phi), \end{aligned} \tag{17}$$

where the first and second terms describe the contributions of the pressure and shear stress forces, respectively. The dimensionless quantities $\tilde{p}$ and $\tilde{\sigma}_{\rho\phi}$ are defined as

$$\tilde{p}=\frac{p}{\tilde{\rho}u_0^2R_0}=\frac{1}{\mathrm{Re}}\int_0^{\phi}d\varphi\,\frac{\partial\omega}{\partial\rho}(\rho=1,\varphi) \tag{18}$$

and

$$\tilde{\sigma}_{\rho\phi}=\frac{\sigma_{r\phi}}{\tilde{\rho}u_0^2R_0}=\frac{R_0}{\mathrm{Re}}[\omega(\rho=1,\phi)+\Omega]. \tag{19}$$

Here $\tilde{\rho}$ is the density of the fluid.

To test the numerical procedure, several runs were carried out for different values of Ω at $\mathrm{Re}=500$ with no controlled vortex present. The time evolution of the drag and lift coefficients was monitored. We have found good agreement [27] with the coefficients measured by Chew *et al.* using a hybrid vortex scheme [28].

IV. FREE-SLIP DYNAMICS AND CONTROL

Before applying the control scheme in a NS flow, we have to determine whether the basic features of the point-vortex flow topology are still preserved in the NS flow. Such an analysis has been presented previously for the free-slip case [19]. Here, we briefly reexamine some of the important results with a control implemented by changing the uniform background flow velocity at infinity.

Previous results on vortex scattering around a cylinder using free-slip dynamics have shown a strong correspondence to the Hamiltonian vortex dynamics [19] if the vortex

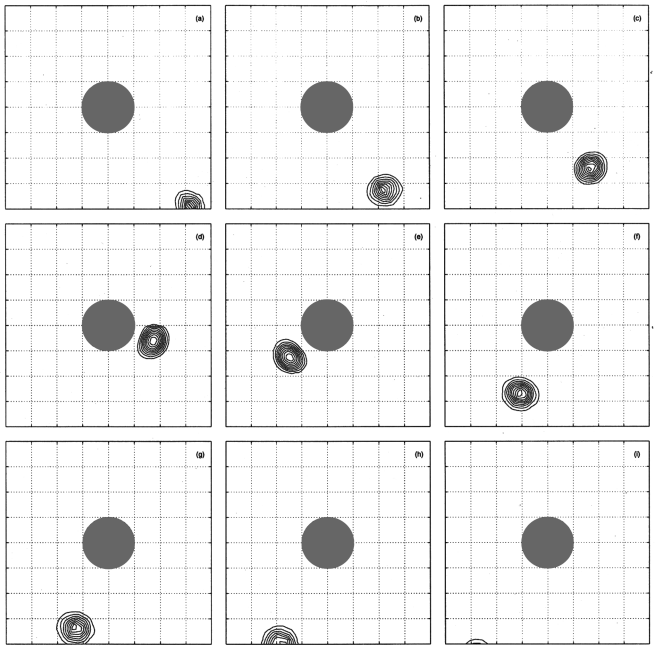

FIG. 4. Time evolution of a small vortex of size $\delta=0.25$, with free-slip dynamics. The vorticity field is shown at time intervals of 2. Constant vorticity lines are shown in increments of $\omega_{\max}/10$. The initial vortex position is (3.0, −4.0), $\sigma=-2.962\,96$, and Re=1000. One grid cell corresponds to a unit square.

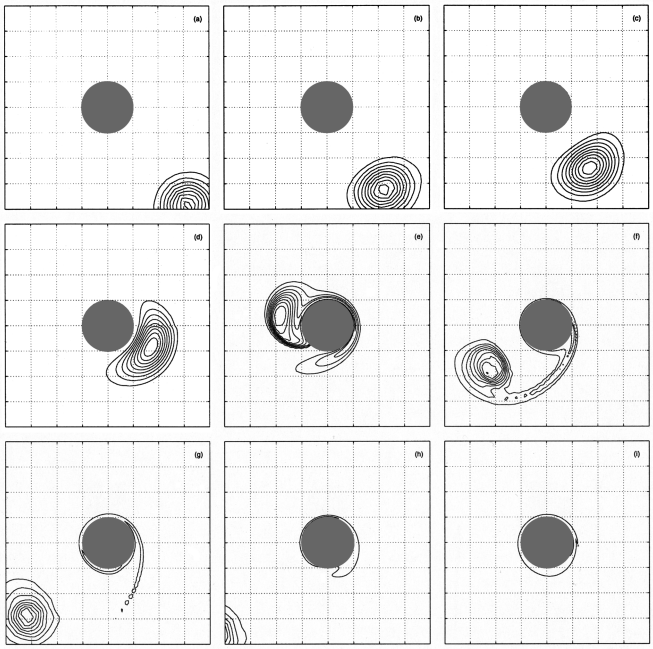

FIG. 5. Time evolution of a large, extended vortex of size $\delta=0.6$, with free-slip dynamics. The vorticity field is shown at time intervals of 2. Constant vorticity lines are shown in increments of $\omega_{\max}/10$. The initial vortex position is (3.0, −4.0), $\sigma=-2.962\,96$, and Re=1000.

patch size is small ($\delta<0.5$). It has been shown analytically in Ref. [19] that the correction to the Hamiltonian dynamical equations is of order η_0^2, where η_0 is a small parameter characterizing possible internal degrees of freedom of the vortex (e.g., ellipticity). This can also be observed in Fig. 4 where the time evolution of the vorticity is shown for an initial patch size of $\delta=0.25$. The Reynolds number is Re=1000. The vortex maintains coherence as it is advected past the cylinder and the center of vorticity closely follows the Hamiltonian trajectory. If the vortex is extended ($\delta>0.5$) the interaction is significantly more complex. This can be observed in Fig. 5, where the vortex dynamics in the case of the free-slip boundary conditions is plotted for a typical initial condition for a large vortex patch of size $\delta=0.6$. During the vortex-cylinder interaction process the initially strongly coherent vortex is stretched, and some low-vorticity filaments detach from the vortex and remain around the cylinder even after the core of the vortex leaves the domain shown in Fig. 5. In this case only the core of the vortex patch of size $\delta=0.6$ maintains coherence and follows roughly the Hamiltonian trajectory [cf. Fig. 6(a)].

Thus we expect that for spatially coherent vortices most of the features of the point-vortex control can be readily implemented for NS free-slip dynamics. The only important inviscid process that cannot be modeled with a simple point-vortex description is the vortex breakdown, when strong shearing fluid motion breaks away a large extended vortex, or some strongly stretched vortex filaments. As we will see below [cf. Fig. 6(d)], however, there are no regions of strong shear in the vicinity of the target saddle point, and these effects do not play an important role during control on time scales shorter than the viscous time.

To achieve control, external perturbations are introduced to the background flow velocity at infinity in the same spirit as for the point-vortex case. The position of the vortex required to evaluate the perturbation is obtained as the center of vorticity of the controlled vortex (15). Thus the action of the controller is determined solely as though a point vortex is present at the center of vorticity of the extended vortex.

To test the validity of the control scheme in the free-slip framework, we place a blob of vorticity with initial condition $(x_0,y_0)=(3,-4)$ and $\delta=0.6$ for Re=1000. A grid of 128×128 is used with stretching parameter $a=0.2$, domain size $\rho_{\max}=100$, and the time step for numerical integration of 0.01. We first evolve the vorticity profile without the control scheme, as shown in Fig. 6(a). One can observe that the core of the blob advects past the cylinder essentially following the Hamiltonian flow lines in spite of the significant shape distortion and detachment of the low-level vorticity. Then we repeat the same numerical experiment, now with the controller turned on [Fig. 6(b)]. The vortex slowly approaches the Hamiltonian fixed point and remains there for at least 30 characteristic flow times. In spite of the fact that the controlled vortex has a slightly distorted shape, the algorithm results in the stabilization of the vortex very close to the fixed point. Figure 6(c) displays the applied perturbation to the uniform background flow as a function of time. After the short targeting period, the required perturbation is small, about 5% of the background flow velocity. With a perfect model of the flow the perturbations would go to zero in the long time limit. The discrepancy is due to the fact that the shape distortions are not included in the point-vortex model on which the control algorithm is based. Note that while an elliptic vortex like the one in the final stages of control is expected to rotate, this one does not have a rotational motion. The absence of rotation can be explained from the to-

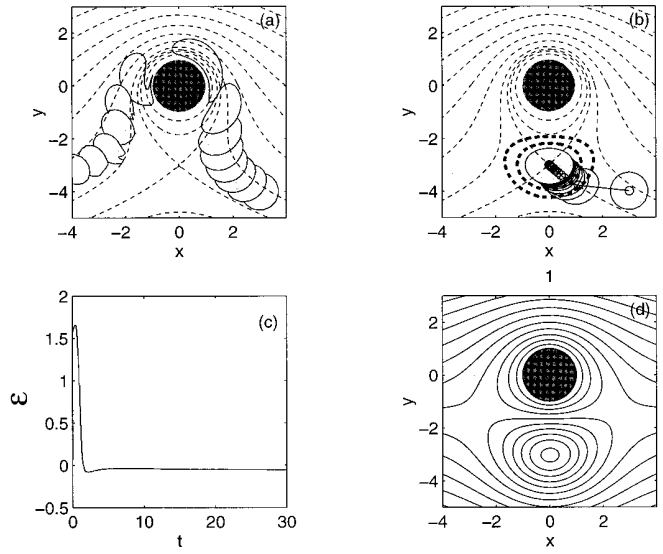

FIG. 6. (a) Evolution of vortex core for the dynamics of an uncontrolled vorticity distribution with free-slip dynamics shown in detail in Fig. 5. The corresponding point-vortex trajectories are shown by thin dashed line. (b) shows the controlled dynamics. The vortex is stably captured at the unstable fixed point of the Hamiltonian flow situated at $(0,-3.0)$ in Euclidean coordinates. As initial conditions, $(3.0, -4.0)$, $\sigma=-2.962\,96$, and size $\delta=0.6$ have been used. One contour level corresponding to $\omega_{\max}/2$ is plotted every unit of time. Thick dashed lines correspond to additional vorticity contours of 0.3 and 0.1 of $\omega_{\max}$ at $t=30$. The figure clearly indicates that the control scheme is stable even for a large vorticity distribution, and a close correspondence with the underlying Hamiltonian system. (c) Time evolution of the control parameter: the perturbation to the background flow velocity. (d) Stream lines of the flow in the controlled case at $t=30$.

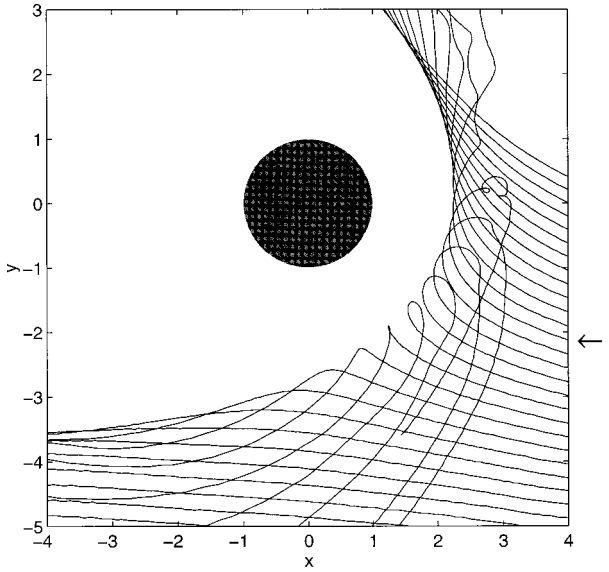

FIG. 7. Vortex scattering with no-slip boundary conditions at $\mathrm{Re}=1000$. The trajectory of the center of vorticity for vortex scattering with different impact parameters is shown for $\alpha=0$. As initial vortex coordinate $x_0=5$, $-6\leqslant y_0\leqslant 0$ has been used. For comparison solid lines in Fig. 3(a) display the vortex trajectories for Hamiltonian dynamics.

pology of the stream lines [Fig. 6(d)], which is essentially similar to the stream-line pattern for a vortex pair [29]. The vortex takes on the shape of the stable stream-line pattern. Figure 6(d) also shows that there is no shearing motion around the controlled vortex and thus the only mechanism by which vorticity can be lost is by diffusion beyond the circular stream-line pattern. On the time scales of our simulation this is minimal and thus there is no significant loss of vorticity during control. This numerical experiment demonstrates that the topology of the underlying Hamiltonian dynamics is still exhibited in the free-slip case. The vortex itself remains stable under the applied perturbations in spite of the shape distortion and diffusion of the original Gaussian vorticity profile.

For the free-slip control the capture time is determined by the viscosity. On viscous time scales the concentrated vortex patch diffuses away and eventually will be broken away by shearing fluid motion. Since this time scale is on the order of 1000 time units we have never been able to reach this stage in our numerical simulations.

V. VORTEX SCATTERING IN A VISCOUS FLOW

We now examine the vortex scattering in the case of no-slip boundary conditions on the cylinder surface, when the cylinder is rotating counterclockwise with uniform angular velocity Ω. This rotation is characterized by the dimensionless parameter $\alpha=\Omega R_0/u_0$, i.e., the ratio of the velocity of the cylinder surface to that of the background flow at infinity. The vortex shedding, drag, and lift coefficients have been extensively analyzed for α values ranging from 0 to 6 [28]. In this section we focus our attention on the dynamics of an external vortex that approaches the cylinder from upstream, interacts with it, and then is advected downstream. Such a vortex could originate from vortices shed by other bodies placed far upstream. This vortex dynamics can be regarded as a kind of scattering process, with a very simple dynamics (uniform advection) far from the cylinder, and a highly nontrivial interaction close to the cylinder. With the initial vortex coordinate x_0 fixed, y_0 can be regarded as an impact parameter that characterizes the scattering process.

There is an additional parameter in the problem, the phase of the beginning of the simulation relative to the periodic vortex shedding. Since the vortex approaching the cylinder strongly disturbs the vortex shedding, we have found that the phase is not an important parameter in the simulation.

Figure 7 displays vortex trajectories with different impact parameters at $\alpha=0$ (no rotation). For comparison Fig. 3(a) displays the vortex dynamics for the Hamiltonian system. The basic difference comes from the vortex–boundary-layer interaction. Figure 8 shows the time evolution of the vorticity field for the trajectory marked in Fig. 7. As the vortex approaches the cylinder on a trajectory similar to the Hamiltonian dynamics, at a critical distance from the cylinder surface a secondary vortex of opposite sign is induced in the boundary layer, which pairs with it and is advected away. Since the strength of the two vortices is not the same, they travel on curved trajectories. The vortex trajectories can typically intersect themselves or other trajectories, since the velocity field depends not only on the actual vortex position but rather on the entire trajectory, i.e., the whole history of the

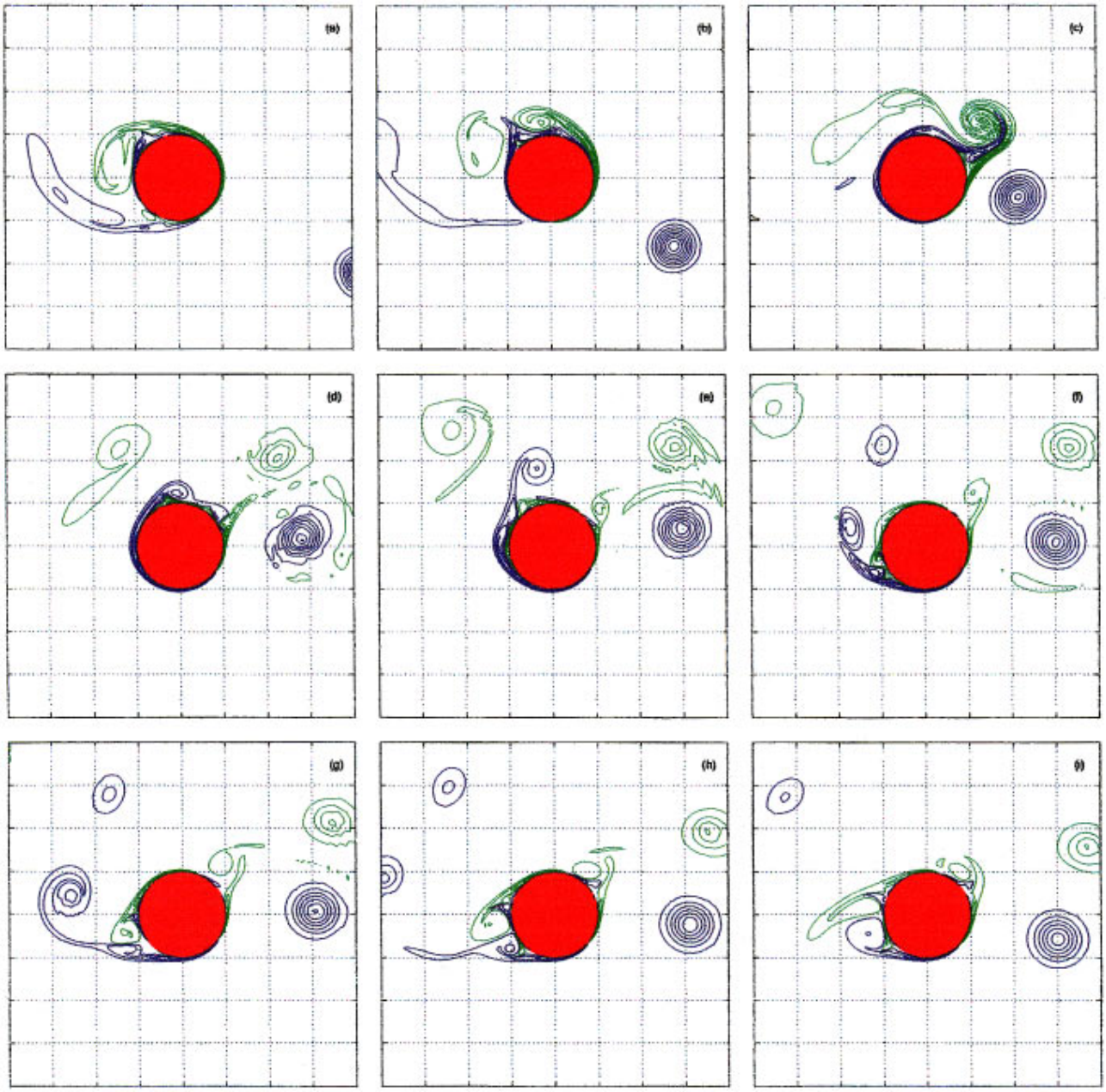

FIG. 8. (Color) Time evolution of the vorticity field for the trajectory marked in Fig. 7. The vorticity contours are shown in green and blue for positive and negative vorticity, respectively. The vorticity increment between consecutive level lines is 5, starting with 2.5 and -2.5 for green and blue lines, respectively. The cylinder is shown in red. The time between consecutive instants of vorticity field is 2. A 256×200 grid has been used in angular and radial direction, respectively, with a step size for integration of 0.001. The stretching parameter was $a=0.2$ and the radius of the computational domain $\rho_{\max}=100$. The size of the initial Gaussian profile was $\delta=0.25$ and the vortex strength $\sigma=-2.962\,96$. One grid cell corresponds to a unit square.

time evolution. Interestingly, Fig. 7 suggests that there is an envelope of these trajectories that defines a region around the cylinder that is not accessible for vortices coming from outside.

Next, we focus on the case of a rotating cylinder. To understand the scattering process in the presence of a rotating cylinder, we recall that the spin up of the surrounding fluid at radius ρ from the origin takes place on a time scale of order $\mathrm{Re}(\rho-1)^2$. Thus the typical time scale can be assumed to be of order of Re. This is much larger than the time a vortex spends around the cylinder before it is transported away by the background flow. Therefore, on relatively short time scales, and for distances not too close to the cylinder surface, the vortex dynamics is not directly affected by the cylinder rotation. The rotation does, however, influence the vortex dynamics through its effect on the stability of the boundary layer. We note here that the cylinder starts to rotate impulsively at time $t=0$, when the vortex is placed upstream of the flow at coordinates (x_0,y_0). Apart from numerical convenience, this seemingly arbitrary relation between the start of the spin and the position of the vortex will be regarded as part of the control action (see next section). The details of the actual vortex dynamics may subtly depend on this choice, but we observe no qualitative differences as long

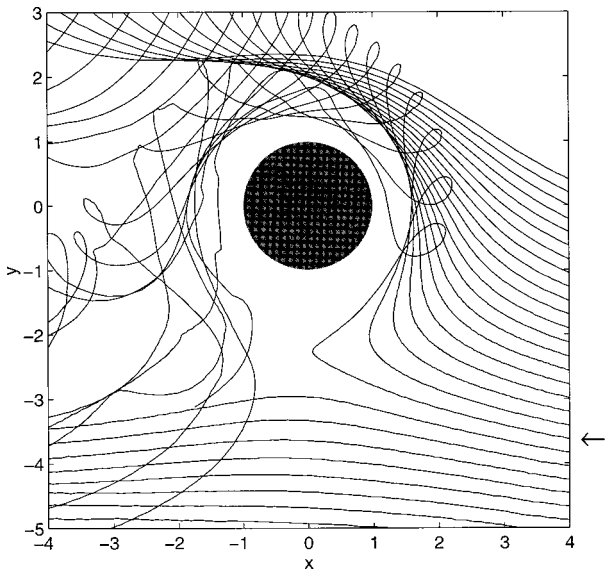

FIG. 9. Vortex scattering with no-slip boundary conditions. The trajectory of vortices with different impact parameters is shown for $\alpha=4$.

as $|\mathbf{r}_0| \ll \mathrm{Re}$ (here $\mathbf{r}_0$ denotes the initial vortex position) [27].

Figure 9 shows the vortex scattering for different impact parameters for a rotating cylinder at $\alpha=4$. One can observe that the vortex can now come significantly closer to the cylinder surface. The trajectory marked with an arrow indicates the existence of a saddle-point-like structure below the cylinder at some instant of time. The time evolution of the vorticity field corresponding to this trajectory is shown in Fig. 10. The boundary layer is stable when the vortex is relatively far from the cylinder surface, but a large positive-signed vortex is shed as the scattered vortex comes close to the cylinder surface.

Figure 11 displays the vortex scattering at $\alpha=10$. Here the overall flow structure has some similarities to the Hamiltonian case, as vortex trajectories typically penetrate the wake of the cylinder. There is a limiting curve for incoming vortex trajectories similar to the separatrix in the Hamiltonian case, that divides trajectories passing below and above the cylinder. One of the significant differences is that several initial conditions lead to a finite-time vortex capture. The time evolution of the vorticity field for one of these captured trajectories is shown in Fig. 12. In the point-vortex dynamics, such finite-time vortex capture has been observed for an oscillating cylinder only. In the Hamiltonian dynamics the origin of such capture is the explicit time dependence of the equations of motion (2) that leads to the formation of a chaotic saddle in the vicinity of the cylinder [20,30,31]. In the case of a viscous flow there is an implicit time dependence of the dynamics due to the vortex–boundary-layer interaction. Moreover, since the captured vortex comes close to the cylinder surface, it is affected by the fluid that is spinning up in the vicinity of the rotating cylinder surface. This also contributes to the fast rotation of the vortex around the body. Note that there is no significant vortex shedding during such a capture process.

In this section we analyzed the vortex scattering on a rotating and translating cylinder in a viscous flow. While the dynamics far from the body is described qualitatively by the Eulerian dynamics, the interaction with the boundary layer as the vortex comes close to the cylinder induces some new interesting effects, i.e., the presence of a region not accessible for vortices approaching from upstream, and also a vortex capturing effect [27]. We plan to present a detailed analysis of this scattering process in future.

VI. VORTEX CONTROL IN THE VISCOUS CASE

The numerical experiments in the preceding section suggest that the boundary-layer dynamics depends strongly on the rotation parameter. The larger the α, the longer is the typical time scale on which a large secondary vortex forms. At large α values the boundary-layer dynamics does not couple with the vortex dynamics. Even at $\alpha=4$, there is no secondary vortex shed as long as the vortex approaching the cylinder is about one cylinder radius away from the cylinder surface. On the other hand, on time scales much smaller than Re, the velocity field at the target fixed point is not affected by the cylinder rotation, and thus our Hamiltonian model (1) is expected to be valid in the vicinity of the fixed point. These arguments have resulted in the following formulation of the control algorithm: let the cylinder be rotating at constant α throughout the control procedure in order to prevent secondary shedding of strong opposite-signed vorticity. Simultaneously, the perturbation to the uniform background flow velocity at infinity δu_0 is changed as a control parameter. The required perturbation is evaluated based on the actual vortex position, assuming the ideal Hamiltonian flow approximation, Eqs. (1), (2), and (8). Such a numerical experiment is presented in Fig. 13. The corresponding control perturbation in the background flow velocity field is shown in Fig. 14.

In Fig. 13, as control is applied the vortex approaches the target saddle point (marked by a cross) along the stable eigendirection. Due to the constant rotation of the cylinder ($\alpha=4$), the vortex shedding gradually diminishes and finally disappears around $t=12$ [plate (g)]. The vortex settles down on the fixed point and remains stable throughout the simulation. Correspondingly, the magnitude of the perturbation slowly decreases, but asymptotically does not reach the zero value. This effect is due to the simple form of the control model of the flow, which does not take into account the additional vorticity in the boundary layer, and to the small but non-negligible effect of the cylinder rotation on the velocity field at the target point. These additional effects lead to a renormalized unperturbed background flow velocity that is slightly smaller than 1, as also suggested by the small negative asymptotic value of the perturbation of -0.3. In fact by estimating the position of the fixed point and the eigenvalues and eigenvectors from the Navier-Stokes scattering simulations, rather than from the Hamiltonian model, one can further reduce the magnitude of the perturbations. Such a simulation is presented in Ref. [27], where the control parameters are extracted from the marked trajectory of Fig. 9. The required perturbations for control are decreased by an additional 50% [27].

During the control procedure the overall controlled vorticity is conserved. The vorticity in a large domain around the controlled vortex changes less than 1% during the control

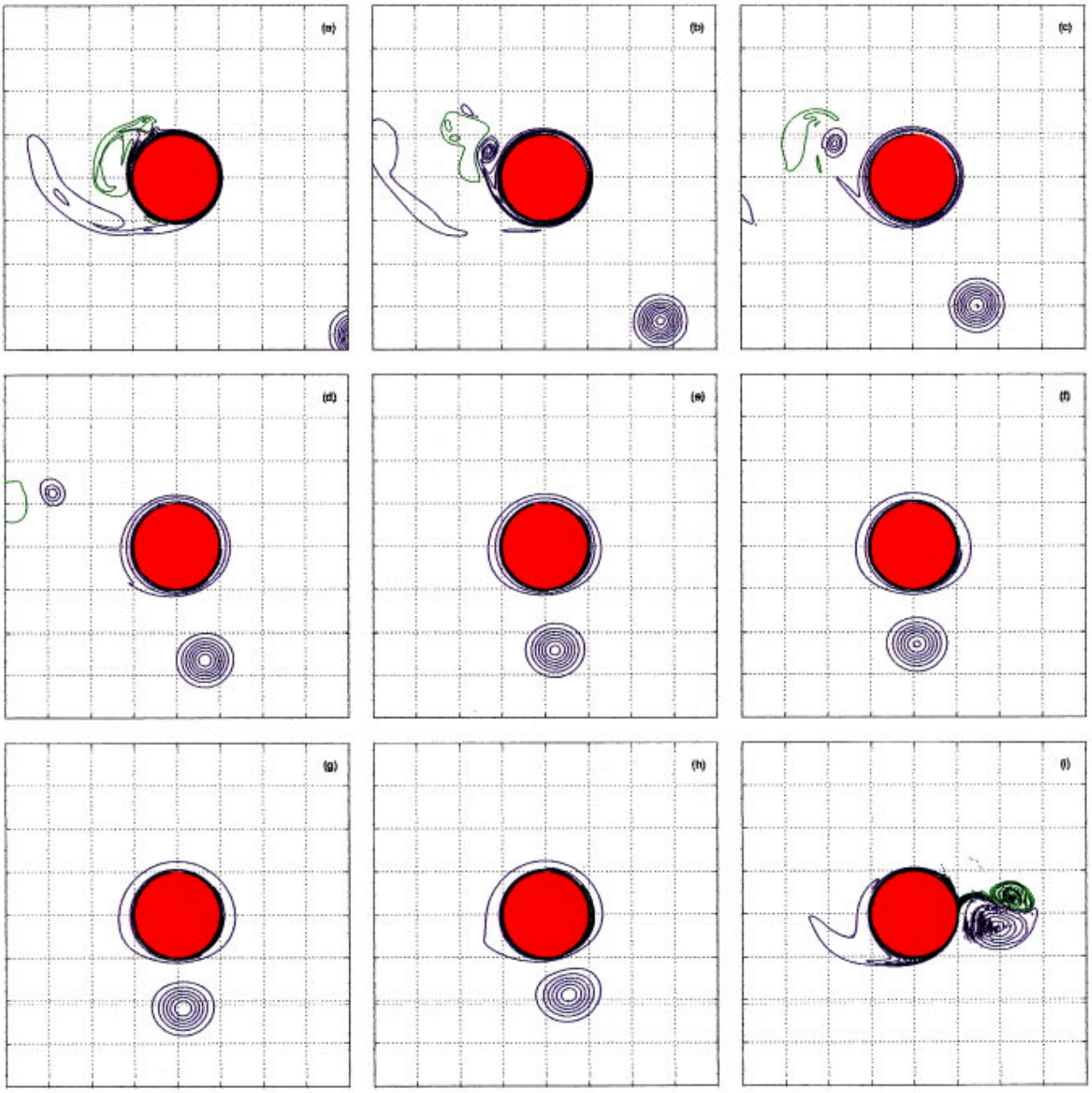

FIG. 10. (Color) Time evolution of the vorticity field with $\alpha=4$ for the trajectory marked by arrow in Fig. 9. The parameters of the numerical solution are the same as those used in Fig. 8.

simulation. The original compact Gaussian vorticity profile, however, diffuses away considerably as shown by the evolution of the vorticity contour lines in Fig. 13.

The time evolution of the drag and lift coefficients is also monitored throughout the numerical experiment. Figure 15 displays these coefficients for various values of α for both the controlled and the uncontrolled state. As a reference, the time evolution with $\alpha=0$ and no controlled vortex present is also shown [Fig. 15(a)]. These are essentially the drag and lift coefficients for a cylinder uniformly translating in a viscous flow. The periodic oscillations are due to the periodic vortex shedding. When the cylinder is rotating counterclockwise with $\alpha=4$ a Magnus effect is observed and the lift coefficient is significantly increased [cf. Fig. 15(b)]. Note, however, that the lift cannot be increased without bound by increasing α. Figure 15(c) shows practically the same asymptotic value for the lift coefficient at $\alpha=10$ as for the one at $\alpha=4$. Also, the ratio of the lift to drag coefficient is actually decreasing from $\alpha=4$ to $\alpha=10$ in accordance with previous observations by Chew *et al.* [28].

Figure 15(d) shows the time evolution of the lift and drag coefficients during the control procedure. There are two interesting observations. First, the mean lift coefficient is of negative sign, e.g., the net lift force is toward the captured vortex. If the captured vortex would be of positive sign, the target fixed point would lie symmetrically just above the cylinder and correspondingly, the lift would be toward the vortex and of positive sign. This is similar to the case of a captured vortex over an airfoil, that is known to significantly increase the lift. Secondly, the drag coefficient is positive

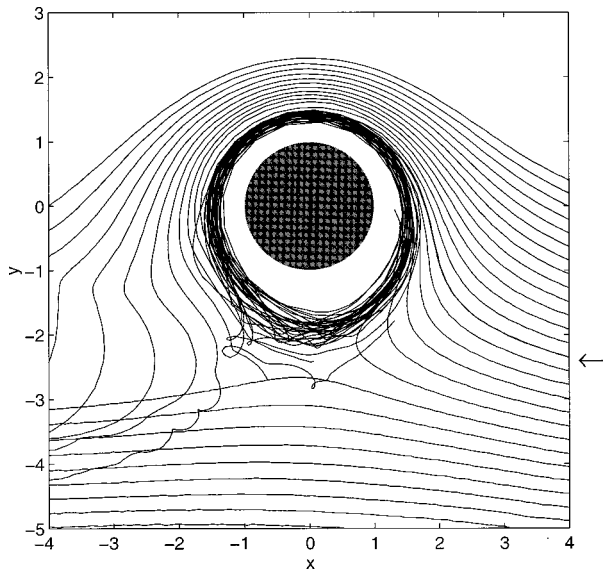

FIG. 11. Vortex scattering with no-slip boundary conditions. The trajectory of vortices with different impact parameters is shown for $\alpha=10$.

and small, which means the body translates practically drag-free and it is even subject to a small thrust. We note that the actual asymptotic value of the lift coefficient in the controlled case is smaller than the one created by a simple Magnus effect at corresponding angular velocities [cf. Figs. 15(b) and 15(d)]. The ratio of the lift to drag coefficient is, however, significantly higher. We note that the controlled vortex-cylinder system shown in Figs. 13(k)–13(p) has a very similar stream function pattern to that of a translating dipole with the controlled vortex being one of the vortices and the cylinder playing the role of the opposite-signed vortex. The forces we obtained in the NS simulations are consistent with such a picture.

Figure 15(e) displays the drag and lift coefficient for a controlled vortex when the cylinder is rotating at constant $\alpha=10$. This shows that the forces do not reach a stationary value, but are oscillating periodically around the value measured in Fig. 15(c) for $\alpha=4$. This is due to the fact that the vortex shedding does not disappear completely, as in Fig. 13, and there is a small shedding of low-level vorticity that leads to the oscillations in the lift and drag coefficients.

The rotation of the cylinder is essential for the success of the control. If the cylinder is not rotating, the vortex can be stabilized for extremely short times only. Soon after the vortex reaches the target saddle point, an opposite-signed vortex is shed from the boundary layer, pairs with the controlled vortex, and subsequently the control fails.

The typical capture time for the no-slip simulations is about 50 time units. On this time scale the boundary layer thickens gradually and eventually a vortex is shed. At this point the control is lost since the shed vortex usually pairs with the controlled vortex and the vortex pair formed cannot be stabilized any longer.

VII. THE VISCOUS RESPONSE OF THE BOUNDARY LAYER

Our goal in this section is to show that there is a steady solution for the boundary-layer equations in the presence of an external vortex, as suggested by the viscous simulations in the preceding section. Previous results on the vortex–boundary-layer interaction show that there are two basic types of response of the boundary layer when a vortex passes close to a wall [32]. In the first case, when the vortex speed is relatively low, there is no steady viscous solution. Secondary vortical structures develop on the wall, leading to an eruption of the boundary layer [33,34]. In the second case, when the vortex moves fast relative to the wall, there is a stable solution, although the boundary layer ''thickens'' gradually [35,36]. Here we show that the long-term stability of the boundary layer observed in the experiments in Sec. VI is due to an effect more subtle than the one leading to the typical stable behavior mentioned above.

When analyzing the viscous response of the boundary layer we assume that the control is active, as shown in Figs. 13(k)–13(p). Therefore the vortex remains stationary, and the cylinder is rotating with a constant angular velocity. For the boundary-layer dynamics, this means that the boundary conditions can be considered as time independent for simplicity.

Let us first introduce the following notations for the velocity components:

$$w=v_r, \quad u=v_\phi \tag{20}$$

for the radial and angular components, respectively, and define the new boundary-layer scaled radial variables

$$\tilde{y}=(\rho-1)\mathrm{Re}^{1/2}, \quad \tilde{w}=w\mathrm{Re}^{1/2}. \tag{21}$$

The Prandtl equations, governing the evolution of the unseparated boundary layer, result as

$$\frac{\partial u}{\partial t}+\tilde{w}\frac{\partial u}{\partial \tilde{y}}+u\frac{\partial u}{\partial \phi}=-\frac{\partial p_\infty}{\partial \phi}+\frac{\partial^2 u}{\partial \tilde{y}^2}, \tag{22}$$

$$\frac{\partial \tilde{w}}{\partial \tilde{y}}+\frac{\partial u}{\partial \phi}=0. \tag{23}$$

Here p_∞ denotes the pressure outside of the boundary layer, due to the inviscid solution at the cylinder boundary in the presence of the background flow and the vortex. The Bernoulli equation implies, for a pressure p_∞ at the outer edge of the boundary layer,

$$dp_\infty=-u_\infty du_\infty. \tag{24}$$

Therefore Eq. (22) expressed in terms of the inviscid velocity u_∞ on the cylinder surface can be written

$$\frac{\partial u}{\partial t}+\tilde{w}\frac{\partial u}{\partial \tilde{y}}+u\frac{\partial u}{\partial \phi}=u_\infty\frac{\partial u_\infty}{\partial \phi}+\frac{\partial^2 u}{\partial \tilde{y}^2}. \tag{25}$$

The boundary conditions are

$$u=\alpha, \quad \tilde{w}=0 \quad \text{at } \tilde{y}=0 \tag{26}$$

and

$$u(\tilde{y},\phi,t)\to u_\infty(\phi), \quad \text{as } \tilde{y}\to\infty. \tag{27}$$

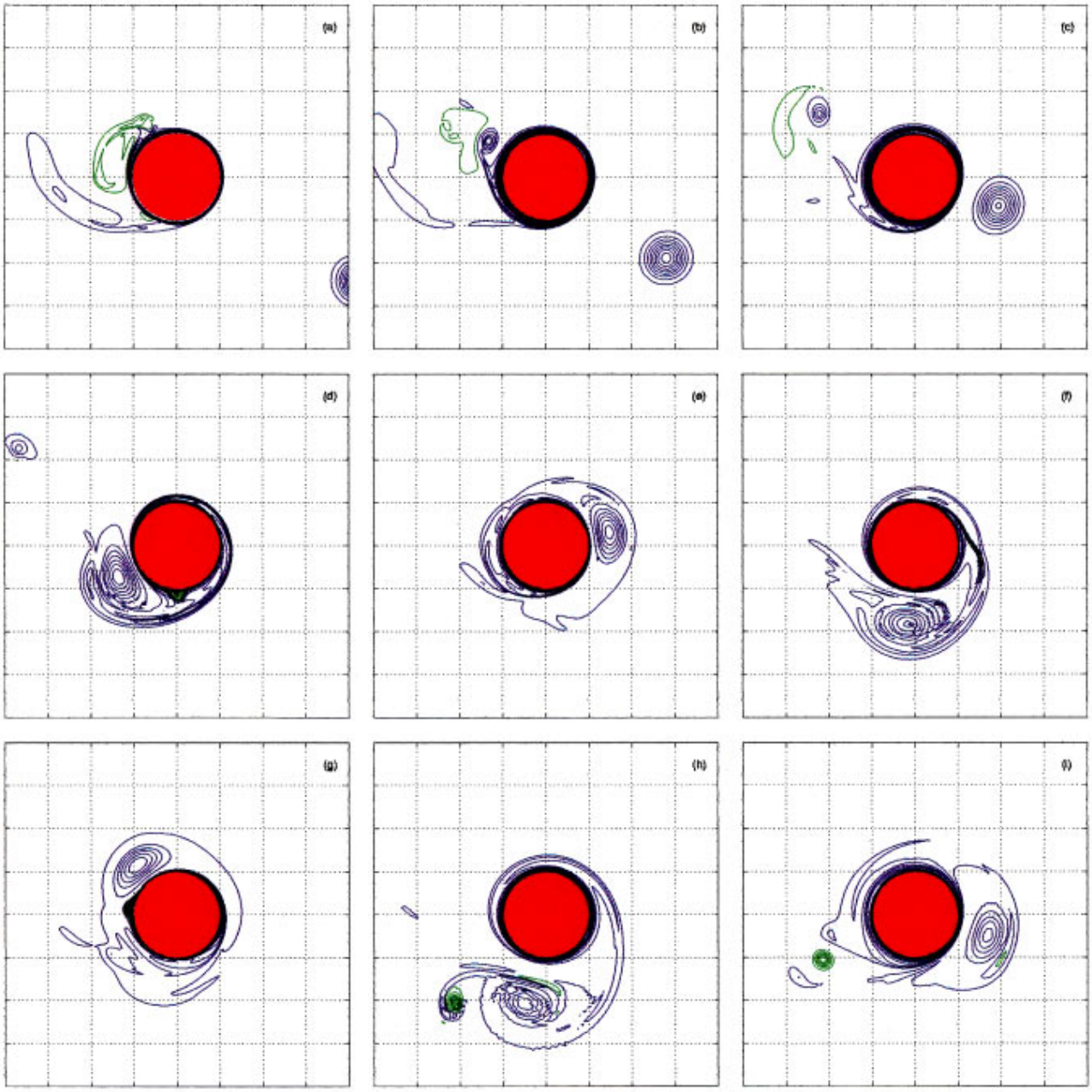

FIG. 12. (Color) Time evolution of the vorticity field for $\alpha=10$ in the case of the trajectory marked by arrow in Fig. 11. The parameters of the numerical solution are the same as those used in Fig. 8.

To increase precision in the physically interesting region near the cylinder wall, we introduce the radially stretched coordinate $\eta=\ln[(\tilde{y}+b)/b]$, with b being a stretching parameter. Then the governing equations (25) and (23) in the new coordinates become

$$\frac{\partial u}{\partial t}+\frac{\tilde{w}}{be^{\eta}}\frac{\partial u}{\partial \eta}+u\frac{\partial u}{\partial \phi}=u_{\infty}\frac{\partial u_{\infty}}{\partial \phi}+\frac{1}{(be^{\eta})^2}\left[\frac{\partial^2 u}{\partial \eta^2}-\frac{\partial u}{\partial \eta}\right], \tag{28}$$

$$\frac{1}{be^{\eta}}\frac{\partial \tilde{w}}{\partial \eta}+\frac{\partial u}{\partial \phi}=0. \tag{29}$$

We solve these equations numerically with a standard finite-difference method. The only input necessary for the problem is α and $u_{\infty}(\phi)$. The angular velocity of the cylinder α is constant, while $u_{\infty}(\phi)$ depends implicitly on the vortex position and background flow. Figure 16(a) shows the typical inviscid velocity profile when the vortex is on the target fixed point and the cylinder is not rotating, i.e., $\alpha=0$. This profile has been obtained as a solution for the inviscid problem with the controlled vortex placed on the target fixed point, and a second opposite-signed vortex placed far downstream, to maintain vorticity balance, as explained before. This profile shows the existence of four stagnation points. One can observe that there is one region with strong adverse pressure gradient (around $1.6\lesssim\phi/\pi\lesssim1.7$) where the secondary vortex is expected to develop [37].

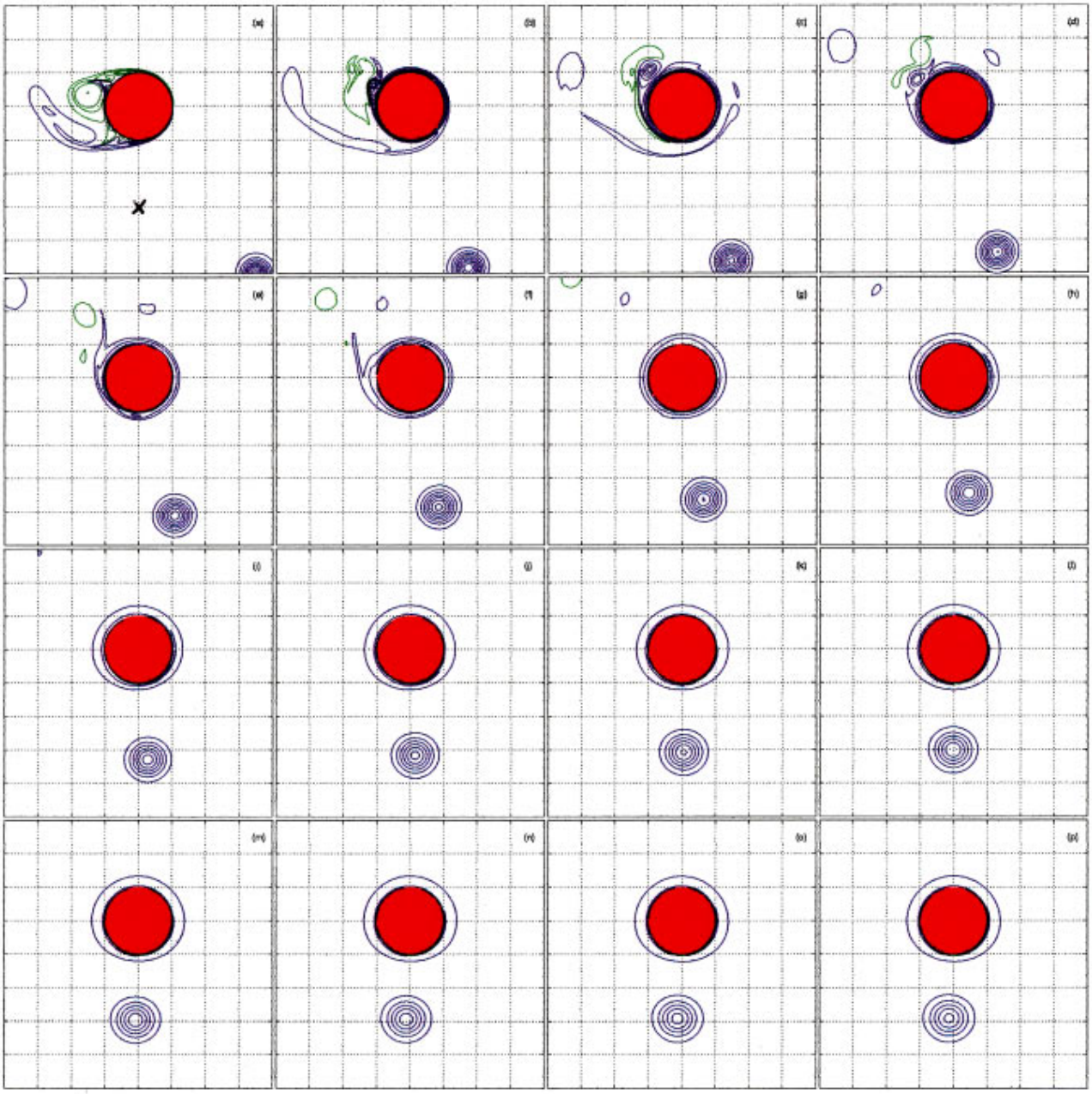

FIG. 13. (Color) Time evolution of the vorticity field in the case of the controlled vortex dynamics with $\alpha=4$. The overall controlled vorticity does not change significantly during the control procedure. The decrease of the number of level lines is due to the fact that the initial compact Gaussian profile diffuses away, i.e., δ increases gradually.

The numerical calculations are performed on a grid 36×64 in radial and angular direction, respectively. The outer boundary is set at a large but finite value $\eta_{\max}=4.0$ with the stretching parameter $b=0.5$. The convergence is checked by repeating the simulation on a larger grid 72×128. No significant differences have been observed.

Figure 16(b) shows the solution to Eqs. (23) and (24) at time $t=0.48$. As an initial condition for the velocity field, we assume that the inviscid solution is valid throughout the boundary. One can observe the newly developed backcirculating structure which later leads to an eruption of the boundary layer as seen in Fig. 8(c). Note that the ''spiky'' appearance of Fig. 16(b) is due to the presence of the stagnation points on the cylinder surface, and the position of flows perpendicular to the surface correspond approximately to these stagnation points.

Figure 16(c) shows the result of the simulation at $t=2.0$ for a rotating cylinder, at the typical value used during the control process $\alpha=4.0$. One can observe the complete absence of the secondary vortical structures, in contrast to the case when the cylinder is not rotating. To understand this remarkable stability of the boundary layer [38], let us transform our problem to a frame comoving with the rotating boundary. The inviscid velocity and pressure profile seen from this frame will be similar to the one in Fig. 16(a), with one difference: in this comoving frame the vortex and the background flow is rotating around the cylinder. This means that the velocity and pressure profile is changing in time

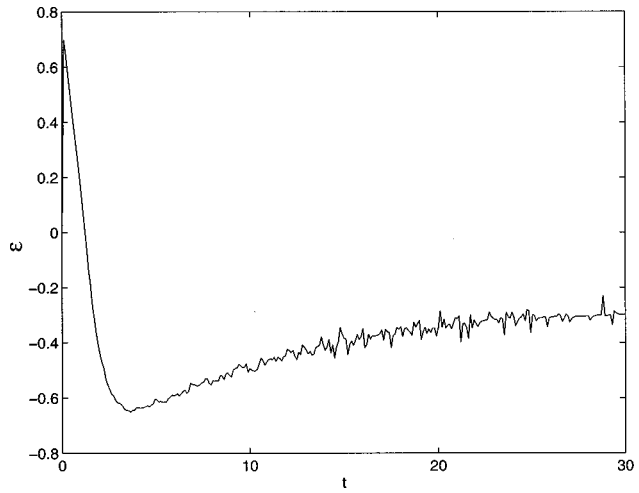

FIG. 14. Time evolution of the control parameter ε during the control procedure shown in Fig. 13.

periodically. The region with positive streamwise pressure gradient from Fig. 16(a) will have a negative pressure gradient just after a period approximately $t_0 \sim \pi/2\alpha$. If the cylinder is rotating fast enough, the outer edge of the boundary

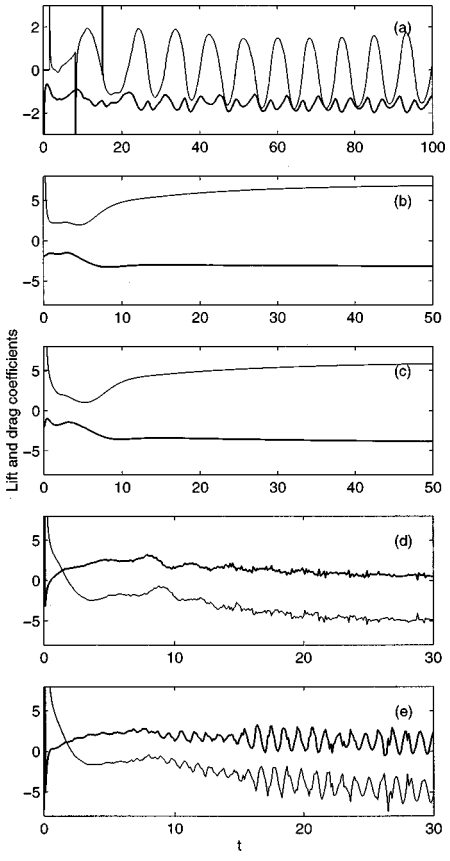

FIG. 15. Time evolution of drag (bold line) and lift (thin line) coefficients for (a) $\alpha=0$, (b) $\alpha=4$, and (c) $\alpha=10$ when no controlled vortex is present. (d) and (e) show the drag and lift coefficients during control for $\alpha=4$ and $\alpha=10$, respectively. Note, that the sign of the coefficients corresponds to the choice of the coordinate system in Fig. 1, i.e., positive drag or lift coefficient corresponds to a force pointing in the positive x or y direction, respectively.

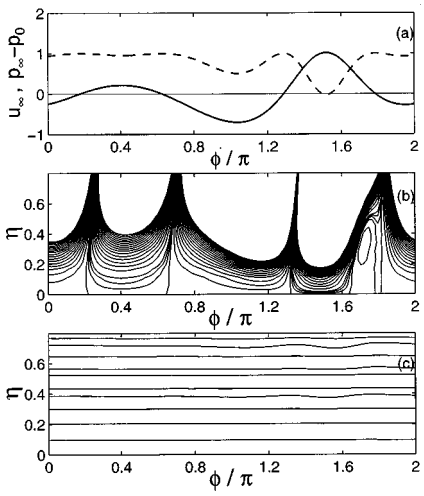

FIG. 16. (a) Inviscid velocity (solid) and pressure (dashed) profile on the cylinder surface for $\varepsilon=0$, with vortex centered on the target fixed point. The pressure is plotted in units of $\rho u_0^2/2$, and p_0 is the pressure at infinity. These profiles have been obtained as the solution to the ''free-slip'' dynamics with a vortex of size $\delta=0.25$ placed on the fixed point. Stream lines of the boundary-layer solution in the laboratory frame: (b) for $\alpha=0$ at $t=0.48$; and (c) for $\alpha=4.0$ at $t=2.0$.

layer experiences an average pressure, without strong gradients. The actual criteria for stability could be formulated in the following way: the typical time scale associated with the generation of the vortical structures in the case $\alpha=0$, that is on the order of $t_v \sim 0.5$, should be larger than t_0. In terms of the cylinder rotation, this means that the angular velocity α should be larger than 1.6. In the limit of large α, the inviscid velocity at the wall seen in the comoving frame $u'_\infty(\phi,t)$ can be replaced by its time averaged value $\langle u'_\infty(\phi,t)\rangle_t$, that in the first approximation is constant and no longer depends on ϕ. In this way, the flow is similar to one occurring between two concentric cylinders, when the inner cylinder is at rest while the outer one is rotating with a relatively low, constant angular velocity.

VIII. CONCLUSIONS

In this paper we studied the interaction of a large coherent vortex with a translating and rotating cylinder. We showed that in a viscous flow, there is an interesting and highly nontrivial scattering effect of advecting vortical structures. Moreover, in the case of a rotating cylinder, these vortices can be captured for long periods. Based on the observations of vortex scattering in viscous flows on the one hand, and a control scheme previously implemented in inviscid flows on the other, we developed a simple control algorithm to stabilize an external vortex near a moving cylinder in a viscous flow.

As a main result, we demonstrated that control of the vortex dynamics based on a low-dimensional reduced dynamical model, previously reported in Hamiltonian and NS ''free-slip'' simulations, can be achieved in a viscous fluid. While previous studies used the circulation around the cylinder as a control parameter, here we introduced a more realistic perturbation: small changes in the uniform background flow velocity at infinity, combined with a uniform

rotation of the cylinder. The perturbation in the background flow velocity corresponds to the change of the velocity of the cylinder translating in a uniform fluid at rest, and can be implemented even in an experiment. The model system shown in this paper is a remarkable example of how some complex fluid flows described by partial differential equations, which are inherently infinite dimensional, can be controlled using a simple low-dimensional model of the fluid flow.

The success of the control is due to the disappearance of the vortex shedding which results from the stability of the boundary layer. We studied this boundary-layer dynamics in detail, and showed numerically that under the applied perturbations the boundary layer is stable, and thus no significant vortex shedding is expected during control. We note here that the same reasoning which leads to stability of the boundary layer in the presence of the controlled vortex can be carried out without the presence of an external vortex, in the case of a rotating and translating cylinder. This suggests that the vortex shedding should disappear at α above some critical value α_c. In fact such disappearance of the vortex shedding has been pointed out in experiments by Jaminet and Van Atta [39] at low Reynolds number flows around a rotating cylinder. Their observation shows that the critical value of the rotation parameter increases with the Reynolds number but has a plateau of $\alpha_c=2$ starting at $\mathrm{Re}\approx 80$, above which the critical rotation velocity no longer depends on the Reynolds number. This result is in qualitative agreement with our explanation, since the boundary-layer argument presented in this section is essentially Reynolds number independent.

In all the successful chaos control experiments presented thus far [13–17], control has been performed without the explicit knowledge of the dynamical equations. The unstable periodic orbits, and their eigenvalues and eigenvectors have been obtained by reconstructing the dynamics directly from time series. In simple open systems like the one studied in this paper, a few scattering trajectories can furnish enough information to reconstruct the dynamics around the saddle point. For example, the marked trajectory in Fig. 9 incorporates all this information with sufficient precision to be used in the control dynamics.

In the present study we restricted our investigation to two-dimensional flows. An interesting question is whether the dynamics of a vortex filament in a three-dimensional flow is stable or not under the control perturbations we apply, or whether instabilities will bend and fold the vortex into a complicated structure. Clearly, more study is needed to answer this question.

Another interesting problem is whether the flow field can be controlled for more generally shaped bodies. In particular, the flow over low-speed airfoils with an attached free vortex has attracted recent interest [40–42]. These works have mainly focused on the stability analysis of the vortex dynamics. Others have studied this problem using a leading-edge flap [43–45] or blowing and suction on the airfoil surface [46] for flow modifications. These attempts, however, are not active control schemes. It is known that unstable fixed points of the vortex dynamics can be found in the Hamiltonian model of a vortex over a Joukowski airfoil [47]. While control of vortex dynamics in such states is possible in the Hamiltonian model system, direct numerical simulation is needed to study the corresponding control problem in viscous flows. In some applications, a vortex stably attached over an airfoil is of primary interest since relatively high levels of lift can be achieved [48]. In other applications, however, the formation and trapping of vortices over airfoil surfaces is not desired, since the detachment of the vortex from the airfoil leads to a sudden decrease of lift, sometimes known as the ''dynamic stall effect'' [32]. In these cases, active control methods could play another role, namely, to prevent metastable capture by driving the vortex toward the unstable direction instead of the stable one.

We must emphasize that, while most point-vortex and inviscid results can be readily extended to more complex bodies using conformal mappings, the viscous results cannot be immediately generalized. The stability of the boundary layer (which is the key to our successful control method) depends strongly on the particular geometry considered. The essential observation is that if a proper mechanism is found that stabilizes the boundary layer (suppresses the vortex shedding), the control of the vortex dynamics in a viscous flow can be successful. At present, there is no reliable way to extract information from the boundary layer which could be used to design a simple controller that stabilizes the boundary layer. This problem remains a continuous challenge for the fluid dynamics and aerodynamics community.

ACKNOWLEDGMENTS

The authors wish to thank L. Cortelezzi, E. Novikov, T. Tél, C. W. Van Atta, and A. Wiegand for very useful discussions. A.P. and J.K. wish to acknowledge partial support for this project by a grant from the Office of Naval Research under Grant No. N00014-96-1-0056, the U.S.–Hungarian Science and Technology Joint Fund under Project JF Nos. 286 and 501, and by the Hungarian Science Foundation under Grant Nos. OTKA T17493 and F17166. G.P. wishes to acknowledge partial support by a travel grant from the NATO Office of Scientific Affairs, under Grant No. SA.5-2-05 (CRG.931160), and the Italian MURST.

[1] M. Gad-el-Hak and D. M. Bushnell, J. Fluids Eng. **113**, 5 (1991).
[2] D. M. Bushnell, Aeronaut. J. **96**, 293 (1992).
[3] M. D. Gunzburger, *Flow Control* (Springer-Verlag, New York, 1995).
[4] R. C. K. Leung, W. F. Chu, S. K. Tang, and N. W. M. Ko, AIAA J. **35**, 802 (1997).
[5] P. Koumoutsakos, Phys. Fluids **9**, 3808 (1997).
[6] L. Cortelezzi, A. Leonard, and J. C. Doyle, J. Fluid Mech. **260**, 127 (1994).
[7] L. Cortelezzi, Y. C. Chen, and H. L. Chang, Phys. Fluids **9**, 2009 (1997).
[8] J. B. Kadtke, Á. Péntek, and G. Pedrizzetti, Phys. Lett. A **204**, 108 (1995).

[9] Á. Péntek, J. B. Kadtke, and Z. Toroczkai, Phys. Lett. A **224**, 85 (1996).
[10] L. R. Keefe, Phys. Fluids A **5**, 931 (1993).
[11] L. R. Keefe, AIAA Paper 93-3279 (1993).
[12] E. Ott, C. Grebogi, and J. A. Yorke, Phys. Rev. Lett. **64**, 1196 (1990).
[13] W. L. Ditto, S. N. Rauseo, and M. L. Spano, Phys. Rev. Lett. **65**, 3211 (1990).
[14] J. Singer, Y. Z. Wang, and H. H. Bau, Phys. Rev. Lett. **66**, 1123 (1991).
[15] V. Petrov, V. Gáspár, J. Masere, and K. Showalter, Nature (London) **361**, 240 (1993).
[16] E. R. Hunt, Phys. Rev. Lett. **67**, 1953 (1991).
[17] R. Roy, T. W. Murphy, Jr., T. D. Mayer, and Z. Gills, Phys. Rev. Lett. **68**, 1259 (1992).
[18] J. B. Kadtke and E. A. Novikov, Chaos **3**, 543 (1993).
[19] H. Luithardt, J. B. Kadtke, and G. Pedrizzetti, Chaos **4**, 681 (1994).
[20] E. Ott and T. Tél, Chaos **3**, 417 (1993).
[21] T. Tél, in *Directions in Chaos*, edited by Hao Bai-Lin (World Scientific, Singapore, 1990), Vol. 3, pp. 149–221.
[22] T. Tél, J. Phys. A **24**, L1359 (1991).
[23] T. Shinbrot *et al.*, Phys. Rev. Lett. **68**, 2863 (1992).
[24] G. Pedrizzetti, J. B. Kadtke, and H. Luithardt, Phys. Rev. E **48**, 3299 (1993).
[25] P. J. Roache, *Computational Fluid Dynamics* (Hermosa, Albuquerque, NM, 1972).
[26] B. Huebinger *et al.* (private communication).
[27] Á. Péntek, Ph.D. thesis, University of California, San Diego, 1998 (unpublished).
[28] Y. T. Chew, M. Cheng, and S. C. Luo, J. Fluid Mech. **229**, 35 (1995).
[29] G. K. Batchelor, *An Introduction to Fluid Dynamics* (Cambridge University Press, Cambridge, England, 1967).
[30] A. Pentek, T. Tél, and Z. Toroczkai, J. Phys. A **28**, 2191 (1995).
[31] A. Pentek, Z. Toroczkai, T. Tél, C. Grebogi, and J. A. Yorke, Phys. Rev. E **51**, 4076 (1995).
[32] T. L. Doligalski, C. R. Smith, and J. D. A. Walker, Annu. Rev. Fluid Mech. **26**, 573 (1994).
[33] J. D. A. Walker, Proc. R. Soc. London, Ser. A **359**, 167 (1978).
[34] G. Pedrizzetti, J. Fluid Mech. **245**, 701 (1992).
[35] T. L. Doligalski, C. R. Smith, and J. D. A. Walker, Prog. Astronaut. Aeronaut. **72**, 47 (1980).
[36] A. J. Bernoff, H. J. H. M. van Dongen, and S. Lichter, Phys. Fluids **8**, 156 (1995).
[37] L. D. Landau and E. M. Lifshitz, *Fluid Mechanics*, Course of Theoretical Physics Vol. 6, 2nd ed. (Pergamon Press, Oxford, 1987).
[38] Here the notion of stability is used in a weak sense, i.e., indicates the absence of shedding, and not the stability of the flow with respect to small perturbations.
[39] J. F. Jaminet and C. W. Van Atta, AIAA J. **7**, 1817 (1969).
[40] P. G. Saffman and J. S. Sheffield, Stud. Appl. Math. **57**, 107 (1977).
[41] P. G. Saffman and S. Tanveer, Stud. Appl. Math. **71**, 65 (1984).
[42] T. W. G. de Laat and R. Coene, J. Fluid Mech. **305**, 93 (1995).
[43] S. Tanveer, Stud. Appl. Math. **72**, 173 (1985).
[44] M. D. Zhou, H. H. Fernholz, H. Y. Ma, J. Z. Wu, and J. M. Wu, AIAA Paper 93-3266 (1993).
[45] V. J. Rossow, J. Aircr. **29**, 847 (1992).
[46] J. F. Slomski and R. M. Coleman, AIAA Paper 93-0864 (1993).
[47] M.-K. Huang and C.-Y. Chow, AIAA J. **20**, 293 (1982).
[48] H. E. Helin, in *Numerical and Physical Aspects of Aerodynamic Flows IV*, edited by T. Cebecci (Springer-Verlag, Berlin, 1990), pp. 229–237.